AIIM

Association for Information and Image Management

1100 Wayne Avenue, Suite 1100
Silver Spring, Maryland 20910

301/587-8202

Centimeter

Inches

MANUFACTURED TO AIIM STANDARDS
BY APPLIED IMAGE, INC.

1 of 1

ANL/ET/CP--82358
Conf-940613--10

CAPABILITIES OF REYNOLDS STRESS TURBULENCE MODEL IN APPLICATIONS TO THERMAL STRATIFICATION*

by

F. C. CHANG AND M. BOTTONI

Energy Technology Division
Argonne National Laboratory
9700 South Cass Avenue
Argonne, Illinois 60439

To be presented at 1994 ASME Pressure Vessels and Piping Division Conference, June 19–23, 1994, Minneapolis, MN

*Work sponsored by U.S. Department of Energy, Pittsburgh Energy Technology Center

CAPABILITIES OF REYNOLDS STRESS TURBULENCE MODEL IN APPLICATIONS TO THERMAL STRATIFICATION

F. C. Chang and M. Bottoni
Energy Technology Division
Argonne National Laboratory
Argonne, Illinois

ABSTRACT

A Reynolds stress turbulence model (RSM) has been implemented in the COMMIX code, together with transport equations describing turbulent heat fluxes, variance of temperature fluctuations, and dissipation of turbulence kinetic energy. This article outlines the model, explains the verifications performed thus far, and discusses potential applications of the RSM in the analysis of thermal stratification in engineering systems. The problem of analyzing thermal stratification and minimizing the impact of thermal stresses on structures is of concern in both nuclear and conventional industries.

INTRODUCTION

In the safety analysis of advanced fast breeder reactors, licensing authorities require that inherent safety capabilities be proved by numerical simulation with well-validated computer programs. Even in the worst case of loss of power to the primary pumps, natural convection circulation must provide, through intermediate heat exchangers, a heat sink sufficient to prevent coolant temperatures from reaching saturation and triggering development of a two-phase flow domain with subsequent reduction of coolant capabilities and loss of core integrity.

Numerical simulations of reactor coolant behavior require the modeling of turbulent flows in the critical transition phase between forced and natural convection. Also required is the modeling of impact of coolant temperature stratification on turbulence, which can be enhanced or suppressed according to unstable or stable stratification patterns. Therefore the accuracy of computer codes depends on the mathematical modeling, particularly on the modeling of turbulence in thermal stratification.

In the critical transition phase between forced and natural convection, turbulence models based on two equations (as is the k-ε model) are inadequate because they assume isotropic behavior of turbulence; this assumption does not hold in complex situations. Therefore, new and detailed modeling is necessary of nonisotropic turbulence in three-dimensional natural convection flows with temperature stratification. This requires a refined evaluation of the interaction between turbulence and buoyancy forces, because this interaction affects both incompressible fluids (because of hydrostatic force gradients) and compressible fluids (where density depends on temperature and pressure).

This paper describes the implementation and evaluation of the Reynolds stress turbulence model (RSM) in the general-purpose multidimensional thermohydraulic computer code COMMIX-1C [1]. This computer code is designed to perform steady-state and transient, single-phase, three-dimensional analysis of fluid flow with heat transfer in engineering systems. COMMIX-1C was developed to analyze heat transfer and fluid flow processes in thermal-hydraulic systems. It is designed in a generalized fashion so that with little or no modification, it can be used to analyze processes in any engineering equipment. This code has provided the framework for the extension of the standard k–ε turbulence model to a more sophisticated model based on 11 transport equations for the dependent variables describing turbulence: six transport equations for the components of the Reynolds stress tensor, three equations for scalar turbulent heat fluxes, one equation for variance of temperature fluctuations, and one equation for dissipation of turbulence kinetic energy. The complete

Reynolds stress model is presented in detail in the next section. The new code version is referred to as COMMIX-1C.RSM.

The objective of this study is to evaluate the intensity distributions of temperature fluctuations related to thermal stratification and to confirm the model's applicability based on analysis of thermal stratification in a rectangular cavity.

ANALYTICAL MODEL

The COMMIX-1C.RSM code solves the conservation equations of mass, momentum, and energy, as well as the 11 transport equations of turbulence, in a finite-difference form. Addition of the Reynolds stress model can make computations more realistic. The turbulence transport equations and the conservation equations for energy and momentum, used in combination with the Reynolds stress model, are given below.

The transport equations for scalar heat fluxes are

$$\frac{\partial}{\partial t}\left(\overline{u_i\phi}\right) + U_j\frac{\partial}{\partial x_j}\left(\overline{u_i\phi}\right) = \frac{\partial}{\partial x_j}\left[\left(\nu_\ell + c_{s\phi}\frac{k^2}{\varepsilon}\right)\frac{\partial\left(\overline{u_i\phi}\right)}{\partial x_j}\right] + P_{i\phi} + G_{i\phi} + \pi_{i\phi}, \quad (1)$$

with

$$P_{i\phi} = -\left(\overline{u_iu_j}\frac{\partial T}{\partial x_j} + \overline{u_j\phi}\frac{\partial U_i}{\partial x_j}\right), \quad (2)$$

$$G_{i\phi} = -\beta g_i\overline{\phi^2}, \quad (3)$$

$$\pi_{i\phi} = -c_{1\phi}\frac{\varepsilon}{k}\overline{u_i\phi} + c_{2\phi}\overline{u_j\phi}\frac{\partial U_i}{\partial x_j} + c_{3\phi}\beta g_i\overline{\phi^2} - c_{1\phi}\frac{\varepsilon}{k}\overline{u_a\phi}\delta_{ia}f\left(\frac{L}{x_a}\right). \quad (4)$$

The transport equation for variance of temperature fluctuations is

$$\frac{\partial g}{\partial t} + \frac{\partial\left(U_jg\right)}{\partial x_j} = \frac{\partial}{\partial x_j}\left[\left(c_\phi\frac{k^2}{\varepsilon} + \frac{\lambda}{\rho c_p}\right)\frac{\partial g}{\partial x_j}\right] - \overline{u_j\phi}\frac{\partial T}{\partial x_j} - \frac{\varepsilon}{k}\frac{g}{R}. \quad (5)$$

The values of R and other model constants are given at the end of this section.

The transport equations for Reynolds stresses are

$$\frac{\partial\left(\overline{u_iu_j}\right)}{\partial t} + U_\ell\frac{\partial\left(\overline{u_iu_j}\right)}{\partial x_\ell} = \frac{\partial}{\partial x_\ell}\left[c_k\frac{k^2}{\varepsilon}\frac{\partial\left(\overline{u_iu_j}\right)}{\partial x_\ell} + \nu_\ell\frac{\partial\left(\overline{u_iu_j}\right)}{\partial x_\ell}\right] - (1-c_2)\left(\overline{u_iu_\ell}\frac{\partial U_j}{\partial x_\ell} + \overline{u_ju_\ell}\frac{\partial U_i}{\partial x_\ell}\right) - \left[\frac{2}{3}\varepsilon\delta_{ij} + c_1\frac{\varepsilon}{k}\left(\overline{u_iu_j} - \frac{2k}{3}\delta_{ij}\right)\right] - \frac{2}{3}c_2\overline{u_au_m}\frac{\partial U_a}{\partial x_m}\delta_{ij} - (1-c_3)\beta\left(g_i\overline{u_j\phi} + g_j\overline{u_i\phi}\right) - \frac{2}{3}c_3\beta g_\ell\overline{u_\ell\phi}\delta_{ij}. \quad (6)$$

The turbulence kinetic energy is $k = \overline{u_iu_i}/2$. The transport equation for the dissipation of turbulence kinetic energy ε is

$$\rho\frac{\partial\varepsilon}{\partial t} + \rho U_j\frac{\partial\varepsilon}{\partial x_j} = c_{1\varepsilon}\frac{\varepsilon}{k}\left(P_k + G_k\right)\left(1 + c_{3\varepsilon}R_f\right) - c_{2\varepsilon}\frac{\rho\varepsilon^2}{k} + \frac{\partial}{\partial x_j}\left(\mu_\ell\frac{\partial\varepsilon}{\partial x_j} + c_\varepsilon\frac{\rho k}{\varepsilon}\overline{u_ju_k}\frac{\partial\varepsilon}{\partial x_k}\right). \quad (7)$$

with

$$P_k = \mu_t\left[\frac{\partial U_j}{\partial x_j}\left(\frac{\partial U_i}{\partial x_j} + \frac{\partial U_j}{\partial x_i}\right)\right], \quad (8)$$

$$G_k = -\rho\beta g_i\overline{u_i\phi}. \quad (9)$$

The energy equation is

$$\rho\frac{\partial h}{\partial t} + \rho U_j\frac{\partial h}{\partial x_j} = \frac{\partial}{\partial x_j}\left(\frac{\lambda}{c_p}\frac{\partial h}{\partial x_j} - \rho c_p\overline{u_j\phi}\right) + S_h, \quad (10)$$

and the scalar components of the momentum equation are

$$\rho\frac{\partial U_i}{\partial t} + \rho U_j\frac{\partial U_i}{\partial x_j} = \frac{\partial}{\partial x_j}\left(\mu_\ell\frac{\partial U_i}{\partial x_j} - \rho\overline{u_iu_j}\right) - \frac{\partial p}{\partial x_i} + \rho g_i + D_i. \quad (11)$$

Boundary Conditions

Figures 1 and 2 show the two–layer wall function model used in COMMIX–1C.RSM. When $y_p > y_\ell$, the first node is in the fully turbulent zone and one has

$$k_p = u^{*2}/\sqrt{c_\mu}. \tag{12}$$

$$\varepsilon_p = u^{*3}/(Ky_p). \tag{13}$$

$$u^* = KU_p/\ell n(Ey_p u^*/\nu_\ell). \tag{14}$$

When $y_p \le y_\ell$, the node P is in the laminar sublayer and one has

$$k_p = u^{*2}(y_p/y_\ell)/\sqrt{c_\mu}. \tag{15}$$

$$\varepsilon_p = u^{*3}/(Ky_\ell). \tag{16}$$

The boundary conditions adopted for the scalar fluxes are

$$\left(\overline{u_i\phi}\right)_p = c_\mu \frac{k^2}{\varepsilon}\frac{\partial T}{\partial x_i}, \tag{17}$$

$$-\overline{u_i\phi} = -\frac{\lambda}{\rho c_p}\frac{\partial T}{\partial x_i} = -\frac{\mu_t}{\rho\sigma_t}\frac{\partial T}{\partial x_i}, \tag{18}$$

for $y_p \le y_\ell$ and $y_p > y_\ell$, respectively.

The boundary conditions for the variance of temperature fluctuations are

$$g_p\left(v_p\frac{y_\ell}{y_p} + \frac{\Gamma_{g\ell}}{y_\ell - y_p} + \frac{\Gamma_{gp}}{y_p}\right) = \Gamma_{g\ell}\frac{g_\ell}{y_\ell - y_p}$$

$$+ \Gamma_{gp}\frac{g_w}{y_p} + \frac{(u^*T^*)^2\sigma_t}{2\nu_\ell}y_\ell - \frac{c_g^2}{R\nu_\ell}(u^*T^*)^2 y_\ell, \tag{19}$$

$$g_w = R\sigma_t T^{*2}/\sqrt{c_\mu}. \tag{20}$$

for $y_p \le y_\ell$ and $y_p > y_\ell$, respectively. Equation 19 has been derived by integrating a one–dimensional transport equation, written for a coordinate normal to the wall, over the laminar boundary layer thickness.

The numerical values of the coefficients used in the above equations are as follows: $c_\mu = 0.09$, $c_g = 1.0$, $c_{3\phi} = 0.07$, $c_{1\phi} = 3.1$, $c_{2\phi} = 0.4$, $c_{3\phi} = 0.5$, $c_{1\phi} = 0.5$, $c_\phi = 0.13$, $R = 0.5$, $c_k = 0.09$, $c_1 = 2.8$, $c_2 = 0.47$, $c_3 = 0.47$, $c_{1\varepsilon} = 1.44$, $c_{2\varepsilon} = 1.92$, $c_{3\varepsilon} = 0.8$, $c_\varepsilon = 0.15$, $\sigma_t = 0.9$, $E = 9.0$, $K = 0.42$. Further details about the turbulence model and the boundary conditions used for all transport equations are given in Ref. 2.

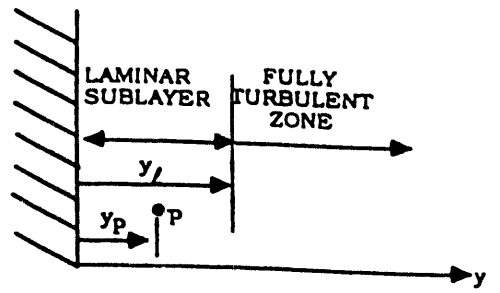

FIG. 1. TWO-LAYER WALL FUNCTION MODEL ($y_p > y_\ell$)

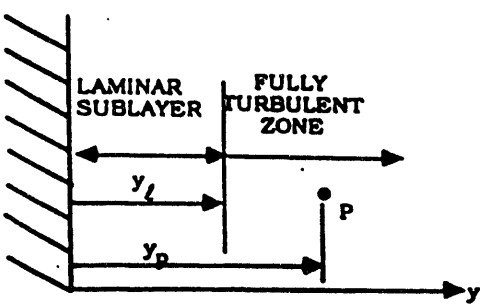

FIG. 2. TWO-LAYER WALL FUNCTION MODEL ($y_p \le y_\ell$)

MODEL VERIFICATION

Homogeneous Turbulent Shear Flow

The condition of homogeneity in turbulence requires an infinite spatial field that can be simulated numerically by a finite domain with slip–free boundary conditions. Early experiments on nearly homogeneous turbulence have been made in wind tunnels during attemps to realize an almost unidirectional flow with a constant velocity gradient. Turbulence generated by grids at the tunnel entrance becomes almost homogeneous in the center of the tunnel at some distance from the inlet. Among the most accurate and best documented experiments on homogeneous turbulence are those by Champagne et al. (Ref. 3), which we chose as a benchmark for validating numerical computations.

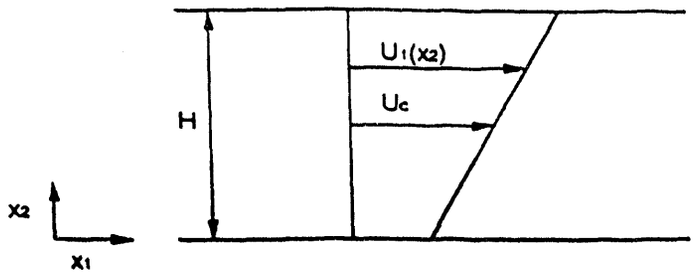

FIG. 3. SKETCH OF HOMOGENEOUS SHEAR FLOW

Specific conditions must be realized in a homogeneous turbulent shear flow. With reference to Fig. 3, let x_1 be a coordinate along the horizontal axis of the wind tunnel. Let x_2 and x_3 be coordinates along the vertical and transverse axis of the tunnel, respectively. Let H be the height of the wind tunnel and $U_c = U_1(H/2)$ be the center velocity. In homogeneous turbulence, the mean velocity components of the flow satisfy the condition

$$U_1 = U_1(x_2), \tag{21a}$$

$$U_2 = U_3 = 0. \tag{21b}$$

$$\partial U_1/\partial x_2 = \text{constant}. \tag{21c}$$

$$\partial U_i/\partial x_j = 0 \qquad (i,j) \neq (1,2). \tag{21d}$$

Under these conditions, the modeled Reynolds equations for homogeneous isotropic turbulence become

$$\frac{d\left(\overline{u_1u_1}\right)}{dt} = -2\overline{u_1u_2}\,\frac{\partial U_1}{\partial x_2} - c_1\frac{\varepsilon}{k}\left(\overline{u_1u_1} - \frac{2}{3}k\right) + \frac{4}{3}c_2\,\overline{u_1u_2}\,\frac{\partial U_1}{\partial x_2} - \frac{2}{3}\varepsilon, \tag{22a}$$

$$\frac{d\left(\overline{u_2u_2}\right)}{dt} = -c_1\frac{\varepsilon}{k}\left(\overline{u_2u_2} - \frac{2}{3}k\right) - \frac{2}{3}c_2\,\overline{u_1u_2}\,\frac{\partial U_1}{\partial x_2} - \frac{2}{3}\varepsilon, \tag{22b}$$

$$\frac{d\left(\overline{u_3u_3}\right)}{dt} = -c_1\frac{\varepsilon}{k}\left(\overline{u_3u_3} - \frac{2}{3}k\right) - \frac{2}{3}c_2\,\overline{u_1u_2}\,\frac{\partial U_1}{\partial x_2} - \frac{2}{3}\varepsilon, \tag{22c}$$

$$\frac{d\left(\overline{u_1u_2}\right)}{dt} = -\overline{u_2u_2}\,\frac{\partial U_1}{\partial x_2} - c_1\frac{\varepsilon}{k}\,\overline{u_1u_2} + c_2\,\overline{u_2u_2}\,\frac{\partial U_1}{\partial x_2}. \tag{22d}$$

$$\frac{d\left(\overline{u_1u_3}\right)}{dt} = -\overline{u_2u_3}\,\frac{\partial U_1}{\partial x_2} - c_1\frac{\varepsilon}{k}\,\overline{u_1u_3} + c_2\,\overline{u_2u_3}\,\frac{\partial U_1}{\partial x_2}. \tag{22e}$$

$$\frac{d\left(\overline{u_2u_3}\right)}{dt} = -c_1\frac{\varepsilon}{k}\,\overline{u_2u_3}. \tag{22f}$$

Under the assumptions of homogeneous turbulence (Eqs. 21a–21d), the equation for the dissipation of turbulence kinetic energy becomes

$$\frac{\partial \varepsilon}{\partial t} = c_{1\varepsilon}\frac{\varepsilon}{k}\left(-\overline{u_1u_2}\right)\frac{\partial U_1}{\partial x_2} - c_{2\varepsilon}\frac{\varepsilon^2}{k}. \tag{23}$$

Because the flow is isothermal, equations (1), (5) and (10) are not solved for this test case.

Numerical Results

Experiments reported in Ref. 3 were made with a center velocity in the wind tunnel $U_c = 12.4$ m/s and with velocity gradient $\partial U_1/\partial x_2 = 13\ s^{-1}$. Measurements were taken in the region defined by $8.5\ H \leq x_1 \leq 10.5\ H$. In the computations, we made numerical calculations of homogeneous turbulence with the RSM in the COMMIX code and with the Runge–Kutta method in an independent program; we then compared the experimental values with the computed results at $x_1/H = 10$ reported in Ref. 3. Experimental and computed results are given in Table I. Under the assumptions made, u_1u_3 and u_2u_3 are negligibly small. The computed results are much closer to each other than to the experimental values, due to the difficulty of realizing in practice the theoretical conditions of homogeneous turbulence. Theoretically, it must be $u_2u_2 = u_3u_3$, a condition satisfied by the results of the calculations but not strictly verified in the experiment. This comparison provides satisfactory verification of the RSM under the given conditions.

Another interesting comparison between experimental and theoretical results can be made in terms of the diagonal components of the tensor a_{ij}, representing the anisotropy of turbulence. This comparison is given in Table II. In Ref. 4 the Reynolds equations for homogeneous isotropic turbulence have been modeled in two different ways referred to as Model 1 and Model 2 in the table.

The only component of the turbulence kinematic viscosity tensor that can be defined under the above given conditions of homogeneous turbulence is

$$\nu_{t12} = -\frac{\overline{u_1 u_2}}{\partial U_1/\partial x_2}. \qquad (24)$$

The computed value was $\nu_{t12} = -(-0.0155)/13 = 1.19 \times 10^{-3}$ m^2/s, which compares with the value $\nu_{t12} = 1.32 \times 10^{-3}$ m^2/s reported in Ref. 3. Using $\nu_\ell = 1.45 \times 10^{-5}$ m^2/s (as in Ref. 3), we obtain the turbulence Reynolds number $Re_t = \nu_t/\nu_\ell = 82$, which compares with $Re_t = 91$ of Ref. 3.

Table I. Experimental and computed turbulence values in homogeneous shear flow (Experimental data present considerable scatter, therefore mean values have been evaluated)

Turbulence Value	Experiment	Calculations	
		Runge–Kutta	COMMIX-RSM
k	0.053	0.030	0.0330
$\sqrt{k}/U_c$	0.0185	0.0139	0.0147
$\sqrt{\overline{u_1u_1}}/U_c$	0.0178	0.0140	0.0143
$\sqrt{\overline{u_2u_2}}/U_c$	0.0132	0.0097	0.0106
$\sqrt{\overline{u_3u_3}}/U_c$	0.0141	0.0097	0.0106
$\sqrt{\lvert\overline{u_1u_2}\rvert}/U_c$	0.0104	0.0101	0.0100
$P_k/\rho = -\overline{u_1u_2}\frac{\partial U_1}{\partial x_2}$	0.218	0.203	0.201

Stratified Shear Flow

In several engineering systems, including advanced nuclear reactors of the pool type, it is important to analyze the effect of fluid stratification on turbulence and to predict under which operating conditions natural circulation flows can become established. Because turbulence in stratified flows is highly anisotropic, the standard k-ε model (which assumes isotropy) performs poorly and must be replaced by more sophisticated models, such as the RSM. This domain of applications is exemplified by the case described below, which provides further verification of the RSM. An experiment designed to study the effect of buoyancy on turbulent mixing is the case of a horizontal shear flow [5], as sketched in Fig. 4. This figure shows qualitatively the spreading of the region where two fluids mix upon entering the domain with different temperatures and velocities. The influence of buoyancy is measured by the reduced Froude number

$$F_r = \frac{|U_2 - U_1|}{\sqrt{g_z \beta\, h |T_2 - T_1|}}. \qquad (25)$$

where the subscript z refers to the vertical component of the acceleration of gravity. In stable stratification, when the hot fluid enters at the top, gravity forces oppose the diffusive character of turbulence, which tends to mix the fluids despite their density differences. The smaller the Froude number, the

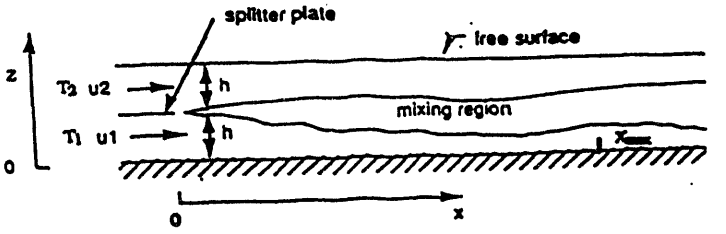

FIG. 4. SKETCH OF STRATIFIED SHEAR FLOW

Table II. Experimental and theoretical values of main diagonal components of a_{ij} tensor

a_{ij} Component	Theoretical Models[4]		Experiment	Calculations	
	Model 1	Model 2	Ref. 3	Runge–Kutta	COMMIX-RSM
$a_{11} = \frac{1}{k}\left(\overline{u_1u_1} - \frac{2}{3}k\right)$	0.30	0.35	0.25	0.35	0.29
$a_{22} = \frac{1}{k}\left(\overline{u_2u_2} - \frac{2}{3}k\right)$	−0.18	−0.175	−0.16	−0.175	−0.145
$a_{33} = \frac{1}{k}\left(\overline{u_3u_3} - \frac{2}{3}k\right)$	−0.12	−0.175	−0.09	−0.175	−0.145

more stable the stratification. Below some threshold of the Froude number, turbulence is completely inhibited by the density gradients. In unstable stratification, when the hot fluid enters at the bottom, the effects of gravity and turbulence combine, forcing a region of highly effective mixing between the hot and cold fluids.

In this study, we used 100 meshes (Δx = 0.03 m) in the axial direction along the channel length and 30 meshes (Δz = 0.006667 m) in the transverse direction. The maximum length (x_{max}) in the x direction is 3 m and the distance (2h) between two plates is 0.2 m. Therefore, the length-to-height ratio (x_{max}/h) is 30. We present results of a test case with unstable stratification and Froude number 0.9, in which hot water is injected at the lower half of the test section, with $U_1 = U_2/2$ = 0.223 m/s, T_1 = 128.7°C, T_2 = 20°C.

Figure 5 shows the temperature distributions at location x/h = 20. With strong mixing, the temperature distributions in hot and cold fluids become almost uniform, displaying a slight temperature inversion with higher temperatures at the top. This temperature inversion is predicted in the calculation made by the RSM, while the k-ε two-equation model fails to reproduce it. Therefore, compared with the k-ε turbulence model, the RSM can produce results closer to the experimental results by accounting for anisotropy of natural circulation and turbulence transport.

The distributions of k at locations x/h =10 and x/h = 20, respectively, are shown in Fig. 6. The distributions of ε at the same locations are displayed in Fig. 7. These two figures show that along the channel, both k and ε are transported from the interface to the interior of the fluids by natural circulation and turbulence. The values of k at x/h = 10 from the RSM are higher than those from the k-ε model. This is because in the RSM, strong contributions to the production of turbulence kinetic energy come from buoyancy. At x/h = 20, the values of k predicted by the RSM become much smaller than those computed with the k-ε model, because strong mixing has already occurred and the temperature distributions become almost uniform, as explained above. The same tendency is recognizable for the dissipation of turbulence kinetic energy.

Figure 8 represents the variance of temperature fluctuations ($g = 0.5\ \phi^2$) at axial locations x/h = 10 , 20, and 30 for the RSM. The variance has a higher value at the interface of two fluids at x/h = 10 and becomes uniform downstream of the channel at x/h = 20 due to the formation of developed flow. The maximum temperature fluctuation (ϕ) at x/h = 10 is about 19°C and seems to be within a reasonable range when compared with the inlet temperature difference [19/(T_2-T_1) = 17%].

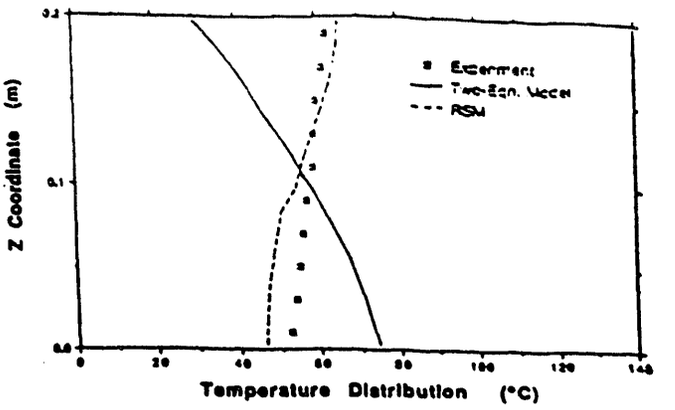

FIG. 5. TEMPERATURE DISTRIBUTIONS FOR UNSTABLE STRATIFIED SHEAR FLOW AT x/h = 20

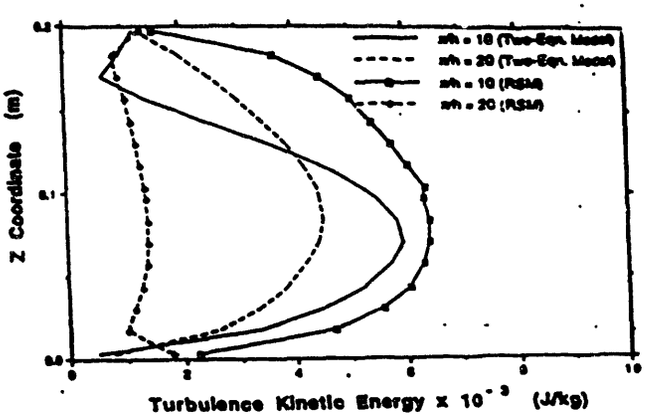

FIG. 6. TURBULENCE KINETIC ENERGY FOR UNSTABLE STRATIFIED SHEAR FLOW AT x/h = 10 AND x/h = 20

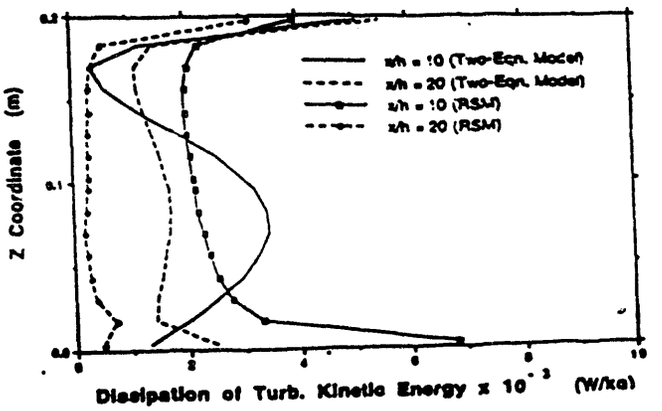

FIG. 7. DISSIPATION OF TURBULENCE KINETIC ENERGY FOR UNSTABLE STRATIFIED SHEAR FLOW AT x/h = 10 AND x/h = 20

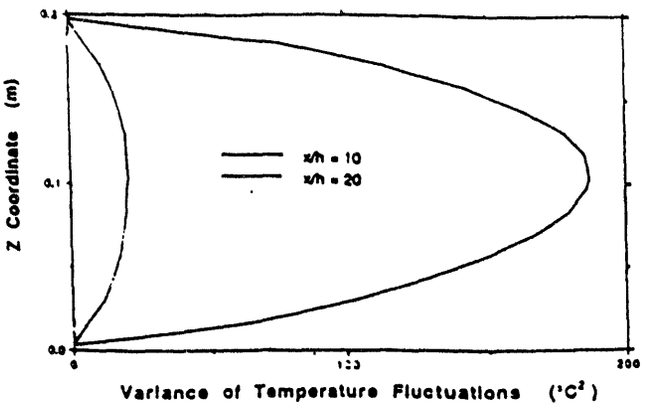

FIG. 8. VARIANCE OF TEMPERATURE FLUCTUATIONS FOR UNSTABLE STRATIFIED SHEAR FLOW AT x/h = 10 AND x/h = 20

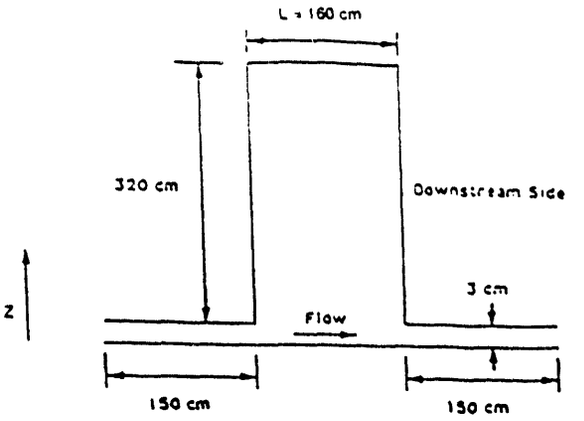

FIG. 9. SKETCH OF THERMAL CAVITY

Thermal Stratification Analysis

For validation of the Reynolds stress model, this study covers the temperature-stratified liquid sodium flow that may occur in a primary reactor vessel under certain operating conditions. In pool-type reactors, liquid sodium coolant is circulated through large pool volumes and the core delivers hot sodium in the hot plenum. Flow conditions through the hot plenum are highly complex, involving jet zones and recirculating currents where the sodium flows at velocities significantly lower than those of the main stream, i.e., those at the core outlet.

During certain operating transients, core outlet temperature may change rapidly with time. An emergency shutdown, for example, results in a sharp temperature reduction. These temperature variations result in density changes that may affect flow conditions, particularly in regions of low velocities. The buoyancy effect may cause thermal stratification characterized by fluid distribution into layers with increasing temperature from the bottom up. Once established, stratification conditions may last a long time.

A good understanding of these stratified flows is important for the design of the submerged structures (e.g., vessels and components), because thermal stress must be included in the analysis in order to determine the overall mechanical loading. Measurements of intensities and frequencies of temperature fluctuations have been made in the safety analysis of nuclear reactors with appropriately chosen Reynolds and Peclet numbers. However, experimental evaluations aiming at accessing the influence of mass flow ratio inside fuel and control assemblies on intensities and frequencies of temperature fluctuations are very costly. Numerical computations are more economical for parametrical analysis. For this purpose, the k-ε turbulence model, which does not compute temperature fluctuations, has been replaced by the RSM in combination with computations of turbulent heat fluxes and of variance of temperature fluctuations.

Thermal stratification experiments have been made in a rectangular cavity filled with liquid sodium and simulating the hot plenum of a liquid–metal fast breeder reactor under steady–state and transient conditions [6]. The cavity is connected at the bottom to a rectangular channel (Fig. 9). A forced flow through the channel induces recirculation in the cavity. The temperature differences are induced in two ways: (a) in the steady state, by heating one of the cavity walls (downstream side) while the other walls remain adiabatic; and (b) in transient conditions, by gradually lowering the temperature of the fluid flowing through the channel while all the cavity walls remain adiabatic.

It is assumed that in the temperature range considered, the Boussinesq approximation holds, i.e., the liquid sodium may be considered as an incompressible fluid with very low thermal expansion. Flow parameters are related to the following scales: (a) characteristic temperature difference ΔT; in the steady state, this is the difference between the temperature of the heating wall and the temperature at the channel inlet while in the transient case, it corresponds to the temperature drop at the channel inlet; (b) cavity width L; and (c) average flow velocity, V_0, in the test section inlet channel.

In the steady-state and transient test cases, some parameters are varied to account for different physical phenomena [7]. The Reynolds number, $R_e = \rho V_0 L/\mu$, expresses the relative importance of inertial and viscous forces on the flow. The Richardson number, $R_i = |\vec{g}| \beta \Delta T L/V_0^2$, expresses the relative importance of inertial forces and buoyancy forces caused by temperature changes within the fluid. The Peclet number, $P_e = \rho c_p V_0/\lambda$, expresses the relative effects of convection and diffusion heat transfer on the temperature field. In the case of a transient where the inlet temperature varies with a time constant τ, the Strouhal number, $S_r = V_0 \tau/L$, is used to compare the time constant τ with flow convection time L/V_0. The time constant τ is based on the initial rate of the thermal transient at the channel inlet.

Results and Discussion

Steady-state tests

The steady-state cases have been investigated with heat transfer through the downstream vertical wall. Vertical temperature profiles in the cavity are presented in dimensionless form: $\overline{T} = f(\overline{z})$ with $\overline{z} = z/L$ and $\overline{T} = (T - T_0)/\Delta T$, where T_0 is the inlet temperature and ΔT is the temperature difference defined above. The main physical parameters, characterizing the steady-state tests chosen for the code validation, are summarized in Table III.

The comparison between experimental and numerical results obtained from the two steady-state cases can be illuminated by considering the influence of the Richardson number on the flow pattern in the cavity. When the Richardson number is small, as in test A1, the flow pattern in the cavity is determined by the strong convective transport, while buoyancy forces are negligible. The cavity becomes filled with an isothermal eddy and the temperature profile is expected to be almost uniform. Conversely, when the Richardson number is high, as in test A2, buoyancy forces are dominant with respect to convection. Thus, the recirculating eddy that determines the mixing between cold fluid in the bottom channel and the hot fluid in the cavity is restricted to a limited region in the bottom of the cavity (about one-third of the cavity height in test A2). The upper region of the cavity (about two-thirds of the cavity height in test A2) is filled with almost stagnant fluid at a temperature close to that of the heated wall. Heat is transferred through this nearly stagnant region almost entirely by conduction, convection heat transfer being negligible.

From the standpoint of comparison between the numerical results obtained with the k-ε turbulence model and the RSM, the following might be expected: In test A1, with low Richardson number and dominant convection heat transfer, a

Table III Main characteristics of steady-state tests

Test No.	P_e	R_i	ΔT (°C)	V_0 (m/s)
A1	4.1e+4	0.03	16.2	1.85
A2	6.9e+3	2.20	33.4	0.29

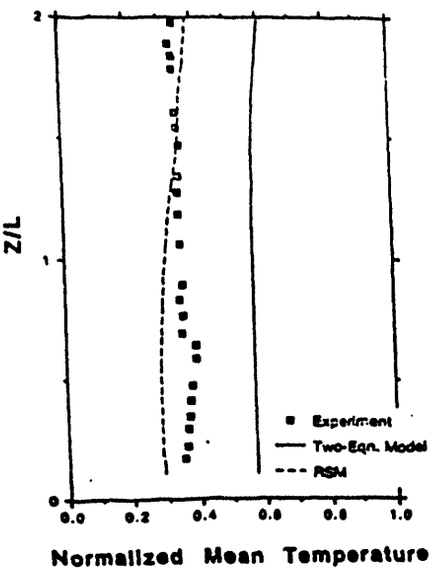

FIG. 10. NORMALIZED MEAN TEMPERATURE DISTRIBUTIONS FOR TEST A1

significant difference between results obtained with the k-ε model and the RSM is expected, because the RSM accounts for the anisotropy of the turbulence stresses in the strong eddy flows. This is confirmed by the normalized mean temperature distributions shown in Fig. 10, in which temperatures refer to a vertical line 200 mm distant from the left wall of the cavity. The results obtained with the RSM are compared in this figure with those of the k-ε model and with the experimental data. In both computed cases, the temperature is rather uniform in the cavity, but the results from the RSM are closer to the experimental data. The differences of the computed temperature distributions depend on the different flow patterns shown in Figs. 11 and 12 for the k-ε model and the RSM, respectively. In both cases, due to strong convection and negligible buoyancy effect, the cavity is filled with only one large eddy, but the centers of the vortices are in very different locations, being much lower in the the RSM calculation.

In test A2, with high Richardson number and low convection heat transfer, the RSM is not expected to give results significantly different from those of the k-ε model. This is also confirmed by the normalized mean temperature

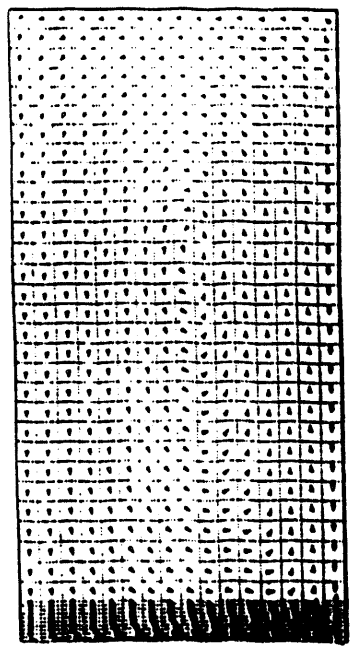

FIG. 11. FLOW PATTERNS OF TEST A1 FOR k-e TWO-EQN. MODEL

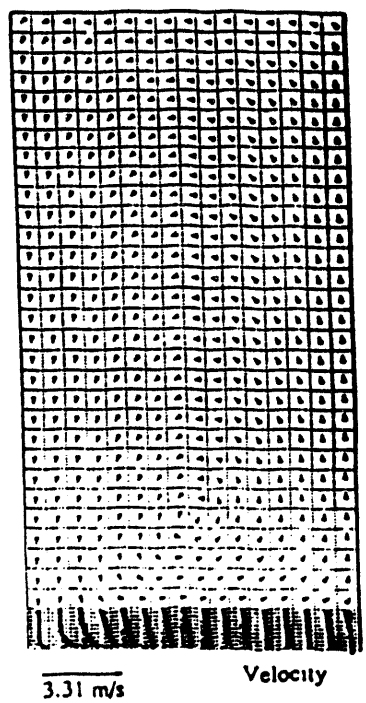

FIG. 12. FLOW PATTERNS OF TEST A1 FOR RSM

distributions shown in Fig. 13. The results obtained with the k-e model and with the RSM are close to each other and are in relatively good agreement with the experimental values.

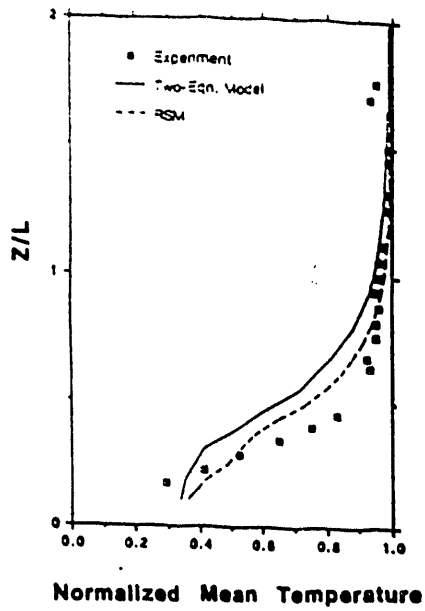

FIG. 13. NORMALIZED MEAN TEMPERATURE DISTRIBUTIONS FOR TEST A2

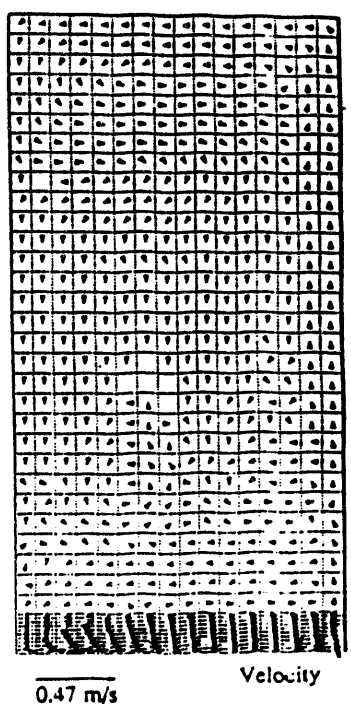

FIG. 14. FLOW PATTERNS OF TEST A2 FOR RSM

Figure 14 shows the flow pattern obtained with the RSM when the lower recirculating eddy is limited to the bottom part of the cavity. The computed results are in agreement with the behavior expected from the phenomenological analysis of the experimental conditions explained at the beginning of this section.

Transient tests

The transient test case has been performed by gradually decreasing the temperature of fluid at the inlet. Characteristic scales L and V_0 have been selected as in the the steady-state case. The only difference is in the characteristic temperature difference ΔT, which is now the magnitude of the temperature drop at the channel inlet. The main physical parameters, characterizing the transient test T2 of Ref. 6 and chosen for the code validation, are summarized in Table IV.

Selected and smoothed experimental data, showing temperatures of some vertical levels in the cavity, 200 mm from the right-hand wall, are shown for comparison in Fig. 15. Computed results with the k-ε model and with the RSM are shown in Figs. 16 and 17, respectively. Analysis of the experimental data, explained in Ref. 6, has led to recognition of three main phases during the transient, characterized in the cavity by the thermal and dynamic behavior described below.

Stage 1: $0 \leq t < 3$ min. This stage corresponds to the beginning of the transient in which the cavity is initially isothermal (T = 300°C). Due to inertia, the incoming cold sodium mixes only slightly with the hot sodium, but induces flow oscillations and consequently temperature oscillations in the cavity, which are recognizable in both the experimental data and the computational results.

Stage 2: $3 \text{ min} \leq t < 15$ min. In this stage, effects of buoyancy significantly modify the dynamic field by opposing the initial momentum of the cold fluid on the isothermal fluid in the cavity. A new flow pattern appears with a small recirculating eddy in the lower part of the cavity, separated from the lighter fluid in the upper part. The temperature of the recirculating eddy decreases to an asymptotic value. This stage ends when the temperature of the recirculating flow becomes almost constant. This phase is recognizable in the computed results of Figs. 16 and 17 between the time in which the temperature perturbations reach the uppermost location of the cavity and the time in which the lowermost temperature plots approach the bottom plateau.

Stage 3: 15 min ≤ t. This stage is characterized by the mixing of hot and cold fluids in the whole cavity. Mixing is controlled by heat conduction from the upper part of cavity to the recirculating eddy in the cavity.

Although a qualitative agreement between computed results and experimental data can be recognized, there are larger discrepancies in the transient case than in the steady-state case

Table IV. Main characteristics of transient tests

Test No.	P_e	R_i	S_r	ΔT (°C)	V_0 (m/s)
T2	2.9e+4	0.15	110	50.0	1.21

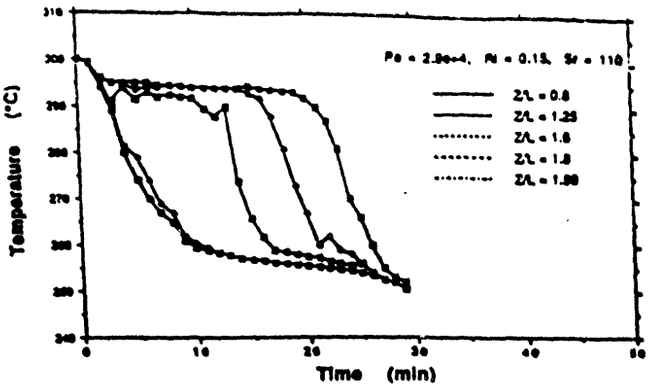

FIG. 15. THERMAL FIELD IN THE CAVITY (EXPERIMENTAL DATA, TEST T2)

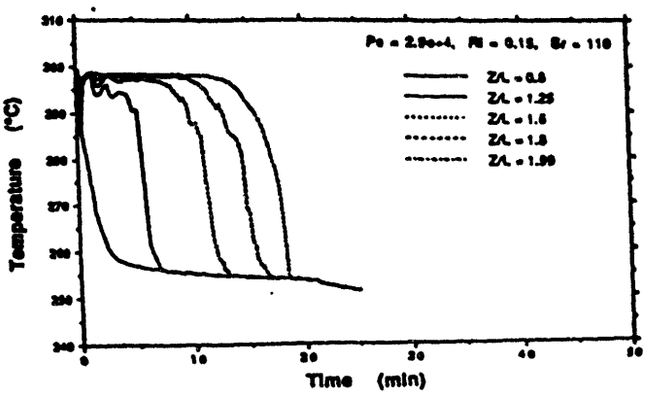

FIG. 16. THERMAL FIELD IN THE CAVITY (k-ε MODEL, TEST T2)

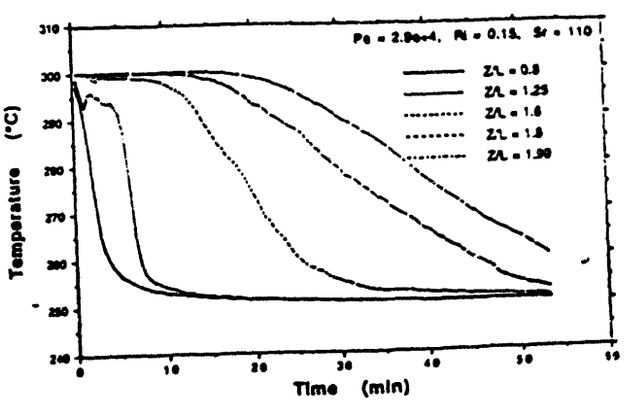

FIG. 17. THERMAL FIELD IN THE CAVITY (RSM, TEST T2)

from the quantitative viewpoint. Let us take as a reference the experimental time-point in which all temperatures in the cavity have dropped to about 255°C. This is about 28 min into the transient. In the calculation made with the k-e model, this time-point is about t = 19 min. It is strongly underestimated, as expected. In the calculation made with the RSM, this time point, about t = 40 min, comes later, as expected, because buoyancy forces are modeled rigorously. The result is, however, an overestimation of the experimentally recorded value. The reasons for this overestimation of the buoyancy forces in the transient case are not well understood at present. The problem must be further investigated by considering other experimental data.

CONCLUSIONS

In all steady-state cases where turbulence is anisotropic, and especially when the enhancement or suppression of turbulence intensity due to buoyancy forces plays a dominant role, the RSM allows more realistic numerical predictions than does the standard k–e model that is based on the inherent assumption of isotropic turbulence. Performance of the RSM in transient cases needs further investigation. The RSM can be applied to a variety of domains of interest for technological applications. Its extension to multicomponent flows is possible, at the expense, however, of high computational costs. To cope with these, more advanced solution algorithms for the transport equations, as well as code parallelization, are envisaged.

NOMENCLATURE

c_p	Specific heat (J/kg–°C)
D	Friction force (kg/m^2-s^2)
E	Constant characterizing the roughness of a boundary surface
F_r	Froude number
G_k	Production or suppression of turbulence kinetic energy due to buoyancy ($J/s–m^3$)
$G_{i\phi}$	Buoyancy production in scalar flux equations (m–°C/s^2)
g	$\left(=\frac{1}{2}\overline{\phi^2}\right)$. One-half of variance of temperature fluctuations ($°C^2$)
$\bar{g}$	Acceleration of gravity (m/s^2)
h	Enthalpy (J/kg)
K	von Karman constant
k	Turbulence kinetic energy (m^2/s^2)
L	Cavity length/Length scale (m)
p	Pressure (N/m^2)
P_e	$(= \rho c_p V_o L/\lambda)$. Peclet number
P_k	Mean shear production in k and ε equations ($J/s–m^3$)
$P_{i\phi}$	Mean field production in scalar flux equations (m–°C/s^2)
q_w	Heat flux from surface ($J/s–m^2$)
Re_t	Turbulence Reynolds number
R_f	$(=-G_k/P_k)$. Flux Richardson number
R_i	$(= g \beta \Delta T L/V_o^2)$. Richardson number
S_h	Source term in energy equation ($J/s-m^3$)
S_r	$(= V_o \tau/L)$. Strouhal number
T	Temperature (°C)
T^*	$(= q_w/\rho c_p u^*)$ (°C)
t	Time (s)
U	Mean flow velocity (m/s)
u	Fluctuation of velocity (m/s)
u^*	Friction velocity (m/s)
$\overline{u_i\phi}$	Scalar heat flux (m–°C/s)
$\overline{u_iu_j}$	Reynolds stress (m^2/s^2)
V_o	Average flow velocity at inlet of channel (m/s)
x_i	Coordinate direction (m)
y_ℓ	Thickness of laminar sublayer (m)
y_P	Distance of node P from the wall (m)

Greek

β	$\left[= -\frac{1}{\rho}\left(\frac{\partial \rho}{\partial T}\right)_p\right]$. Volume expansion coefficient at constant pressure ($°C^{-1}$)
$\Gamma_{g\ell}$	Laminar diffusivity at location y_ℓ (m^2/s)
Γ_{g_p}	Laminar diffusivity at location y_P (m^2/s)
δ_{ij}	Kronecker delta
ε	Dissipation of turbulence kinetic energy (W/kg)
λ	Thermal conductivity (W/m–°C)
τ	Time constant (s)
μ	Dynamic viscosity (kg/m–s)
ν	Kinematic viscosity (m^2/s)
$\pi_{i\phi}$	Pressure–scalar gradient correlation in scalar heat flux equations (m–°C/s^2)
ρ	Density (kg/m^3)
σ_t	Turbulence Prandtl number for heat transport
ϕ	Temperature fluctuation (°C)
$\overline{\phi^2}$	Variance of temperature fluctuations ($°C^2$)

Indices

i	Free or dummy index
j	Free or dummy index

ℓ	Free or dummy index, Laminar
m	Free or dummy index
n	Free or dummy index, Normal to wall
o	Inlet
p	Node P
t	Turbulence

REFERENCES

1. Domanus, H. M. et al., COMMIX-1C: A Three-Dimensional Transient Single-Phase Computer Program for Thermal Hydraulic Analysis of Single and Multicomponent Systems, Volume I: Equations and Numerics; Volume II: User's Guide and Manual, NUREG/CR-5649, ANL-90/33, Argonne National Laboratory, Argonne, IL, 1990.
2. Bottoni, M. and Chang, F. C., Implementation of an Anisotropic Turbulence Model in the COMMIX-1C/ATM Computer Code, Proc. Pressure Vessel and Piping (PVP) Division of ASME Conf., Denver, CO, July 25-29, 1993.
3. Champagne, F. H., Harris, V. G., and Corrsin S., Experiments in Nearly Homogeneous Turbulent Shear Flow, J. Fluid Mech.,Vol. 41 (1970), pp. 81-133.
4. Launder, B. E., Reece, G. J. and Rodi, W., Progress in the Development of a Reynolds Stress Turbulence Closure. J. Fluid Mech., Vol. 46 (1975), pp. 537-566.
5. Viollet, P. L., Turbulent Mixing in a Two-Layer Stratified Shear Flow, 2nd Int. Symp. on Stratified Flows, Trondheim, Norway (1980), pp. 315-325.
6. Vidil, R., Grand, D., and Leroux, F., Interaction of Recirculation and Stable Stratification in a Rectangular Cavity Filled with Sodium, Nuclear Eng. and Design 125 (1988), pp. 321-332.
7. Grand, D., Abadie, P., Martin, R., and Vidil, R., Combined Convection of Sodium in Rectangular Cavity, Nuclear Reactor Thermal Hydraulics Topical Meeting, Saratoga Spring, NY, Oct. 6, 1980.

DATE
FILMED
7/25/94
END